Challenges in determining the thermal conductivity of core-shell nanowires by atomistic simulation

The Journal of Chemical Physics

RESEARCH ARTICLE | MARCH 24 2025

Challenges in determining the thermal conductivity of core–shell nanowires by atomistic simulation

Alireza Seifi ; Mahyar Ghasemi ; Movaffaq Kateb ; Pirooz Marashi

J. Chem. Phys. 162, 124706 (2025)
https://doi.org/10.1063/5.0246759

AIP Publishing

The Journal of Chemical Physics ARTICLE pubs.aip.org/aip/jcp

Challenges in determining the thermal conductivity of core–shell nanowires by atomistic simulation

Cite as: J. Chem. Phys. 162, 124706 (2025); doi: 10.1063/5.0246759
Submitted: 4 November 2024 • Accepted: 2 March 2025 •
Published Online: 24 March 2025

Alireza Seifi,[1] Mahyar Ghasemi,[1] Movaffaq Kateb,[2,a)] and Pirooz Marashi[1]

AFFILIATIONS

[1] Department of Materials and Metallurgical Engineering, Amirkabir University of Technology, 15875-4413, 15916-34311 Tehran, Iran
[2] Department of Physics, Condensed Matter and Materials Theory Division, Chalmers University of Technology, SE-41296 Gothenburg, Sweden

[a)] **Author to whom correspondence should be addressed:** movaffaq.kateb@chalmers.se

ABSTRACT

In the present work, we investigate the thermal conductivity (κ) of different core–shell nanowires using molecular dynamics simulation and Green–Kubo (EMD), imposing a temperature gradient (NEMD) and Müller-Plathe (rNEMD) approaches. We show that in GaAs@InAs nanowires, the interface effect becomes more significant than the nanowire cross-sectional geometry. In particular, κ decreases as the interface area increases, reaching a minimum, and then increases when the interface strain relaxes. This is particularly important for thermoelectric applications, where minimization of κ is desired. In particular, the different methods can predict minima at different core diameters without special considerations. In addition, the NEMD approach and, to a lesser extent, rNEMD tend to overestimate the κ values, which cannot be corrected with the methods available in the literature. By analyzing the temperature and length dependence, (I) we show that interfacial scattering primarily involves phonon–phonon interactions, which mainly affect low-energy modes, a mechanism that effectively reduces κ at low temperatures. (II) The Langevin thermostat tends to pump low-energy modes in the NEMD approach, but this effect decreases with longer nanowires. (III) Energy exchanges in rNEMD stimulate high-energy phonons, derived from the saturation of κ at a much shorter nanowire length than NEMD. These findings highlight the challenges of accurately determining κ of ultrathin core–shell nanowires, where only the EMD approach provides precise results. With the recognition of non-equilibrium contributions to the overestimation of κ by NEMD and rNEMD, these methods can still provide valuable insights for a comprehensive understanding of the underlying thermal transport mechanisms.

I. INTRODUCTION

Thermoelectric devices provide power generation and cooling that have an impact on both energy demand and the environment.[1] In short, a temperature gradient (ΔT) over a thermoelectric material can create a voltage between the hot and cold ends, a phenomenon known as the Seebeck effect. Conversely, by applying a voltage, the heat can be transported away from the target end via the Peltier effect. The efficiency of a thermoelectric material at a given temperature T is quantified by its *figure of merit* (zT),

$$zT = \frac{\sigma S^2 T}{\kappa}, \tag{1}$$

where σ and κ are the electrical conductivity and thermal conductivity and $S = -\Delta V/\Delta T$ is the Seebeck coefficient with ΔV being the open circuit voltage at a small ΔT.

While the search for efficient thermoelectric materials has existed for decades, it has reached its full potential only recently. Advances in nanofabrication and characterization have opened up new avenues for material development. Thermoelectric devices can be scaled down to just a few nanometers, as they contain no moving parts. In the case of small bandgap semiconductors with low electron effective mass (m^*), such as InAs, nanowire structures are predicted to enhance thermoelectric performance by ~50% compared to bulk materials.[2] For example, InAs nanowires exhibit significantly higher

electron mobility (μ)[3] and κ[4] compared to their bulk counterparts, making them a promising thermoelectric material. In this context, both the *power factor* (σS^2) and κ of InAs nanowires have been investigated to optimize the thermoelectric figure of merit, zT.[5–8] In a field-effect transistor (FET) configuration, σ of InAs nanowires exhibits discrete steps with varying gate voltage, a behavior that is more pronounced at 40 K.[5] The authors attributed this observation to 1D quantum confinement effects. However, subsequent studies revealed that σS^2 can be enhanced by an order of magnitude at temperatures below 20 K, which cannot be explained by 1D confinement alone.[6] Likewise, κ of InAs nanowires can be modified through various methods, including Si doping,[8] the introduction of planar defects,[8,9] and altering surface roughness.[9]

Recently, there has been a growing interest in the core–shell nanowires. For instance, InAs@InP nanowires exhibit 2–5 times increase in μ compared to the bare InAs nanowires, which has been attributed to surface passivation.[10] GaAs in the core–shell geometry exhibits an order of magnitude lower κ than that of pure nanowires.[11] Theoretically, applying a strong transverse magnetic field that induces *snaking* and Landau states can reverse the thermoelectric current (from cold to hot) in a thin InAs shell.[12] Using the Landauer–Büttiker formalism, it has been demonstrated that both κ and S, and therefore zT, in InAs shells exhibit oscillatory behavior with the transverse magnetic field.[13] At higher temperatures (above 100 K), however, phonon contributions are dominant,[14] tuning by a magnetic field becomes ineffective, and geometrical effects become more significant.[15] Experimental evidence has shown that Si–Ge core–shell nanowires with diameters between 15 and 20 nm exhibit lower κ than the alloy nanowires.[16] They demonstrated that κ in these nanowires is reduced beyond the diffusive boundary scattering limit using the Boltzmann transport equation (BTE). This suggests that modeling κ of core–shell nanowires using the BTE is particularly challenging, especially for ultrathin nanowires.

Most of the experimental studies mentioned above utilized InAs nanowires with diameters larger than 20 nm. In practice, ultra-thin nanowires suffer from a high density of defects, making their handling infeasible. However, molecular dynamics (MD) simulations have proven to yield meaningful insights for smaller nanowires.[17] MD simulations have shown that [110] InAs nanowires exhibit higher κ than their [100] and [111] counterparts of the same size.[18] As for core–shell nanowires, InAs has been barely studied[19] compared to Si and Ge.[15,20–24] In the Si–Ge system, it has been demonstrated that surface phonons disappear due to the presence of the core–shell interface.[20] However, changes in the phonon density of states (PDOS) away from the surface/interface were negligible, suggesting a minimal impact on κ where surface modes contribute little. Using MD, it has been shown that core–shell geometry causes a coherent resonant of transverse and longitudinal modes for Si/Ge nanowires.[21,22] More recent studies have shown that κ of core–shell nanowires is lower than the average of the individual core and shell materials.[15] For comparison, bulk Si and Ge have κ of 130[25,26] and 58 W/mK,[27–29] respectively, few times higher than systems such as GaAs and InAs, with conductivities of 44[30,31] and 27 W/mK,[29,32] respectively. Furthermore, Si and Ge have a lattice mismatch of 4.2%, leading to relatively small strain at the interface,[33] in contrast to the 7.2% mismatch between InAs and GaAs. Consequently, the heat flux in Si@Ge nanowires is uniform across the cross section,[15,20] while in InAs@GaAs and GaAs@InAs nanowires, heat flux predominantly passes through the GaAs component.[19]

In this study, we investigate κ of nanowires with hexagonal GaAs cores and hexagonal or triangular InAs shells. The fabrication of such nanowires has already been reported for InP@InAs[34] and GaAs@InAs.[35] Building on these studies, we explore different core radii and consider slight rotations to adjust core–shell alignment. We also evaluate κ using several widely used methods, providing useful comparisons with the existing literature while discussing the advantages and challenges associated with each approach.

II. METHOD

A. General MD framework

MD simulations were performed using the `LAMMPS` open source code[36] and `GPUMD`.[37] We utilized the Tersoff[38] three-body potential to describe interatomic interactions. Unlike pair potentials, it accounts for the number of bonds or the so-called coordination number and the change in bond length due to the second nearest neighbor. Thus, it enables describing covalent bonds accurately and is successfully applied for determining κ of C,[39] Si,[15] Ge,[15] and III–V semiconductor[17,19] nanowires. In particular, modeling small nanowires requires a more complex potential such as Tersoff due to the increased sensitivity of vibrational behavior to many-body interactions.[17,40] The general Tersoff potential takes the following form:

$$U(r_{ij}) = f_c(r_{ij})[A_{ij}\exp(-\lambda_{ij}r_{ij}) - b_{ij}B_{ij}\exp(-\alpha_{ij}r_{ij})], \quad (2)$$

with r_{ij} being the distance between atoms i and j; A_{ij}, B_{ij}, λ_{ij}, and α_{ij} being fitting parameters; and f_c being the smoothing function that works near the cutoff. The main bond order term of the Tersoff potential is b_{ij} that changes the attraction based on the bond angle, the number of nearest neighbors, and their symmetry,

$$b_{ij} = \left[1 + (\beta\zeta_{ij})^n\right]^{-\frac{1}{2n}}, \quad (3)$$

$$\zeta_{ij} = \sum f_c(r_{ij})g(\theta_{ijk})\exp\left[\lambda^m(r_{ij} - rik)^m\right], \quad (4)$$

$$g(\theta_{ijk}) = \left(1 + \left(\frac{c}{d}\right)^2 - \frac{c^2}{d^2 + (h - \cos\theta_{ijk})^2}\right)\gamma_{ijk}. \quad (5)$$

Here, α, β, n, m, c, d, and h are fitting constants; some are known depending on the specific Tersoff formalism. We used the latest Tersoff parameters of InGaAs from Ref. 41, which have been fitted to *ab initio* results to produce the correct lattice parameter, elastic modulus, and elastic constant relevant for accurate κ calculation and took into account surface reconstruction and surface energy necessary for modeling nanowires. In addition, it produced the bulk κ accurately and predicted higher κ for pure GaAs than InAs nanowires correctly,[17] while earlier parameters, cf. Ref. 19, predicted κ for GaAs nanowires considerably lower than the InAs ones. The potential utilized here provided stable nanowires with hexagonal and triangular cross sections, except for the occasional back and forth jump at the corners (300–500 K), whereas other potentials needed surface passivation with 1–3 monolayer(s) to avoid As sublimation.[17]

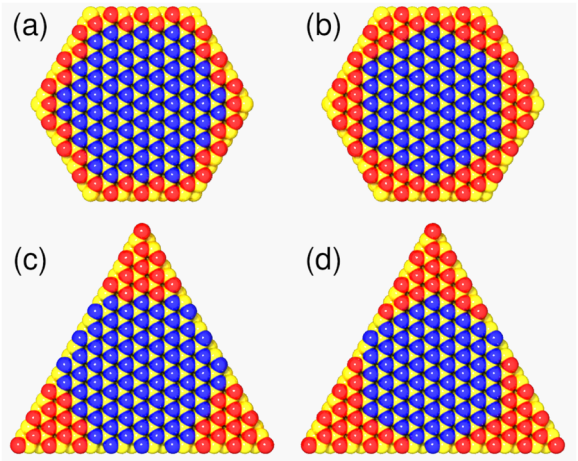

FIG. 1. Cross section of (a) and (c) side-matched and (b) and (d) corner-matched GaAs@InAs core–shell nanowires. Here, red, blue, and yellow atoms demonstrate In, Ga, and As atoms, respectively.

As shown in Fig. 1, we considered two geometries with 0–5 nm hexagonal cores in the hexagonal [(a) and (b)] and triangular [(c) and (d)] shells with the same cross-sectional area. The nanowire's axis is parallel to the ⟨111⟩ orientation and ~50 and 100 nm long. Regardless of the shell geometry, two types of *matching*, i.e., sides of the core are parallel to those of the shell (*side*-matched) and corners of the core pointing at sides of the shell (*corner*-matched), can be defined. Note that the In/Ga ratio is preserved upon the change in the shell geometry, while between the two matchings, the side match presents a lower In/Ga ratio. The nanowires were placed in the middle of a nearly cubic box with periodic boundary conditions in their axial direction and relaxed at desired temperatures (100, 200, 300, 400, and 500 K) to produce zero average stress along their axis. The velocity Verlet[42] algorithm was employed for the time integration of the equation of the motion with a time step of 1 fs. The Nosé–Hoover thermostat is used for temperature control with 100 fs damping. During the relaxation, we allowed changing the box dimension parallel to nanowire's axis every 1 ps to relax stress controlling pressure by using the Nosé–Hoover barostat. This will produce samples from the isothermal–isobaric ensemble (NPT).

For all production runs, we used a microcanonical ensemble (NVE) that does not rescale velocities and allows for thermal fluctuation or temperature profile development along the nanowire's axis.

B. PDOS calculation

To calculate PDOS, we used the Fourier transform of the velocity auto-correlation function, $\langle v(t)|v(0)\rangle$, sampled from the MD trajectory,[43]

$$g(\omega) = \int e^{i\omega t} \frac{\langle v(t)|v(0)\rangle}{\langle v(0)|v(0)\rangle} \mathrm{d}t. \tag{6}$$

To this end, nearly 10 nm long nanowires were considered and sampled every 5 fs for a maximum correlation time of 1 ps with the total sampling time of 1 ns. Further details on the PDOS calibration can be found in Sec. S3 of the supplementary material.

C. Thermal conductivity calculation

The Green–Kubo[44,45] method relates the ensemble average of the auto-correlation of the heat flux to κ,

$$\kappa_{pq} = \frac{1}{Vk_BT^2}\int_0^\infty dt\langle J_p(t)J_q(0)\rangle, \tag{7}$$

where p and q subscripts denote Cartesian components, V is the volume, k_B is Boltzmann's constant, and T is the temperature. $J(t)$ is the heat flux at time t which for solids can be calculated from the fluctuations of per-atom potential energy.

Since the Green–Kubo method is performed at equilibrium, it is sometimes referred to as equilibrium MD (EMD). The most important problem with EMD is its computation cost, i.e., the auto-correlation function needs to become convergent, and for materials with high κ, the correlation time can be a few ns, and for several sampling, its time reaches tenths of ns. In addition, EMD does not require a temperature gradient that makes it sensitive to the choice of initial velocities and requires several sampling with different initial velocities. It has also been debated whether κ measured by EMD represents the exact value along the nanowire axis. These motivated another class of algorithm called non-equilibrium MD (NEMD).

In the NEMD approach, a temperature gradient can be imposed by thermostating two regions at different temperatures or in response to adding and subtracting energy to those regions called reverse NEMD (rNEMD). Then, κ can be calculated using Fourier's law,

$$\kappa = \frac{QL}{\Delta TA}, \tag{8}$$

where Q is the energy transferred in the given time, L is the distance between hot and cold regions with a temperature difference of ΔT, and A is the cross section perpendicular to the transport direction.

Fourier's law requires infinitely small ΔT to remain valid, while, in practice, this causes large fluctuations in ΔT and Q.[46] Instead, a large ΔT is applied over short length (<100 nm) that produces a linear profile away from cold and hot regions. As a result, κ shows a length dependence behavior using NEMD.[47] Müller-Plathe[46] proposed an rNEMD approach based on exchanging kinetic energy between the hot and cold segments to produce ΔT. Thus, the heat flux is already known from the amount of exchanged energy and the temperature profile becomes stable much faster than the other methods.

Here, we compare the results of EMD, NEMD, and rNEMD methods by Müller-Plathe.[46] To determine κ using EMD, sampling was performed every 20 fs for a maximum correlation time of 1 ns with the total sampling time of 10 ns. As dynamic properties are strongly affected by the choice of the initial condition,[48] we performed 20–100 individual runs depending on how well κ is converged. As implemented in `GPUMD`, each run will start with different initial conditions. A more detailed description of the individual EMD samples and their averaging is presented in Sec. S4 of the supplementary material.

For the NEMD calculation, nanowires were divided into ten slices along the nanowire axis: the first slice was fixed as suggested by a GPUMD developer and second and last slices were maintained at ±10 K using the Langevin thermostat with 1 ps damping.

For the rNEMD method, we optimized a number of slices along the nanowire axis with respect to ΔT. We obtained the minimum ΔT to the limit where cumulative exchanged heat remained linear. Then we enlarged slices until a linear temperature profile is produced. We considered ten slices with a periodic boundary condition in that direction for ΔT between 7 and 37 K at different equilibrium temperatures (100–500 K). The latter has been achieved by swapping one cold and hot atom every 1 ps.

The method for calculating ΔT includes sampling T of slices every 10 fs. Then, we averaged 100 samples, and the result was recorded along with slice coordination. Knowing the slices T and their distances, one can calculate multiple $\Delta T/L$ values. We chose two slices at the center and then moved away from the center. Thus, the last slices correspond to cold and hot regions as suggested by Li *et al.*,[49] which give the error bar minimum.

The OVITO package[50] and GPYUMD were used to generate atomistic illustrations and post-processing.

III. RESULTS AND DISCUSSION

A. Stress distribution

Figure 2 shows the distribution of the stress component parallel to the nanowire axis ($\sigma_{//}$) in the nanowire's cross section after relaxation at 300 K. The figure presents an average over time and the nanowire's length obtained without a temperature gradient. Within each subplot, the distribution is plotted with the black solid line with its vertical axis being the normalized count and the horizontal one being $\sigma_{//}$ spanning over the same range as in the color-bar (±9 GPa). Note that the vertical dashed line indicates $\sigma_{//} = 0$ and not the direction where stress is measured. We present these curves separately with more details in Fig. S1 of the supplementary material. For most of the cases, the distribution roughly consisted of two peaks within tensile ($\sigma_{//} > 0$) and compressive ($\sigma_{//} < 0$) regions, indicated by red and blue in the cross section, respectively. Starting from pure InAs in the leftmost column, there is a major peak with negligible tensile stress, an overlapping peak at zero, and a minor peak around −1.5 GPa. Looking at the cross section, we can locate the compressed region at the nanowire's surface, a relaxed layer near the surface, and the interior part with tensile stress, indicated by pale blue, white, and pale red, respectively. A similar but more symmetric stress distribution happens for pure GaAs in the top-right corner. The introduction of the 1 nm core expands the relaxed (white) region corresponding to the major peak at $\sigma_{//} = 0$ and does not change the minor peak due to the nanowire's surface. However, there are small jumps in the distribution at $\sigma_{//} > 0$ because of tensile stress localized at the core. For $D_{core} = 2$ nm, the major peak is completely located in $\sigma_{//} < 0$, which makes the shell almost entirely pale blue, and the core experiences high tensile stress (the minor peak at 8 GPa) evident from dark red. A nearly balanced situation occurs for the 3 nm core where the core and shell experience intermediate but opposite stresses. A further increase in D_{core} gives more weight to the tensile peak due to a larger core and minor peak due to the blue shell gradually vanishing. The rest of the σ components are presented in Figs. S2 and S3 of the supplementary material.

B. Phonon dispersion

Figure 3 shows the variation of phonon dispersion with D_{core} for hexagonal GaAs in the hexagonal InAs shell. Thus, $D_{core} = 0$ and 5 nm indicate pure InAs and GaAs nanowires. The InAs results here are in quantitative agreement with earlier studies obtained by the three-body Stillinger–Weber potential[51,52] but different from results obtained by other Tersoff parameters.[18] It can be seen that $D_{core} = 1$–4 nm does not change transverse acoustic modes at endpoints (Γ and Y) but gradually bends them toward higher frequencies in the middle points (cf. Fig. S4 of the supplementary material). This effect has been attributed to the strain in various systems[53] with the shift magnitude being linearly proportional to the strain.

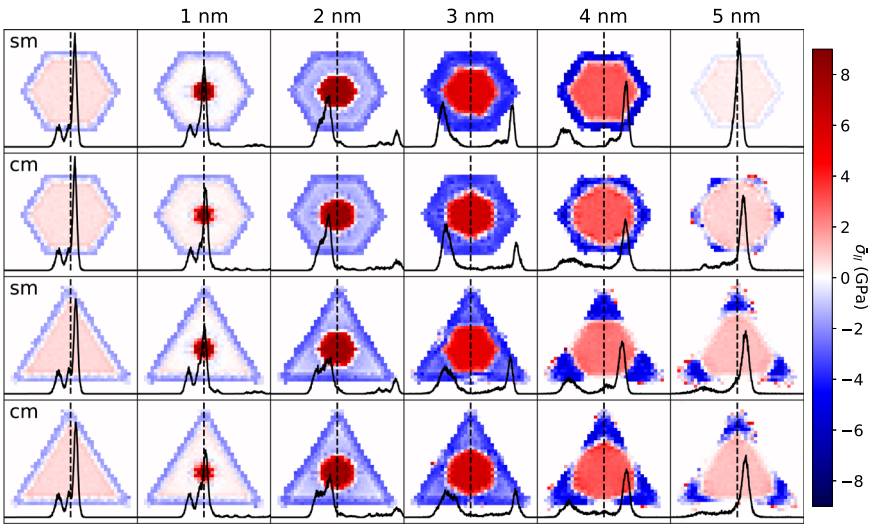

FIG. 2. Distribution of longitudinal stress ($\sigma_{//}$) for different geometries and D_{core} = 0–5 nm, indicated on top, at 300 K. The solid lines indicate distribution, i.e., normalized count vs $\sigma_{//}$ in the ±9 GPa range (see also Fig. S1 of the supplementary material). Note that the dashed line indicates $\sigma_{//} = 0$ for the black solid line and not the direction of measurement. The color bar is true for all subplots.

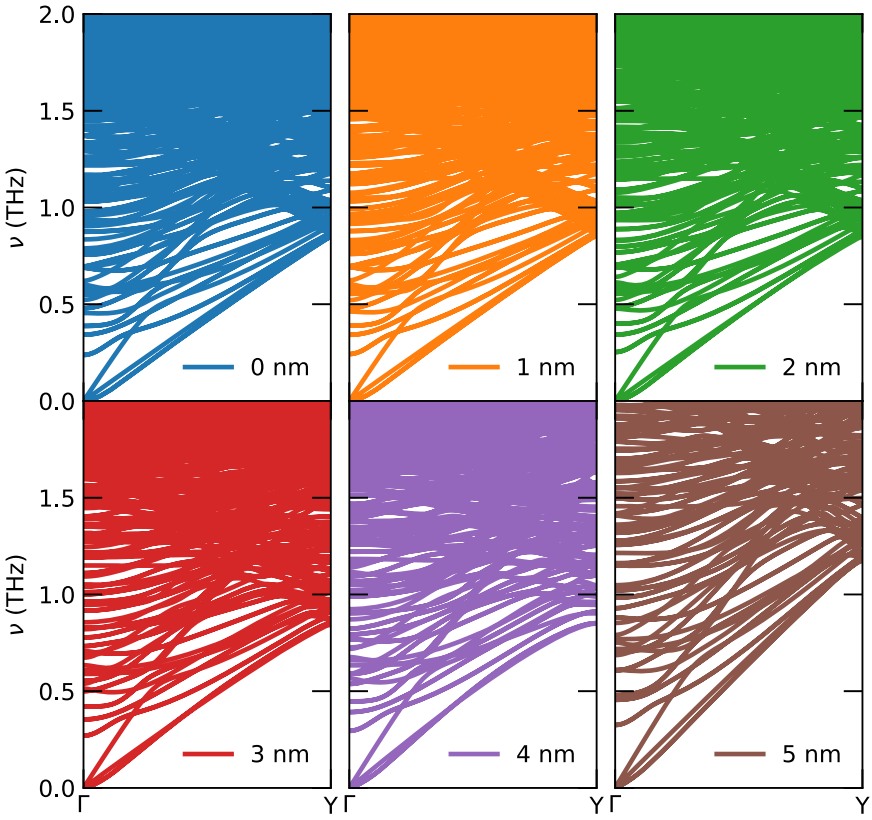

FIG. 3. Phonon dispersion of 0–5 nm hexagonal GaAs@5 nm hexagonal InAs and side-matched alignment.

It is also worth mentioning that in $InGa_xAs_{1-x}$, where In is randomly replaced with Ga, the Y point value changes with x.[54] For the rest of the modes, including longitudinal acoustic modes, a shift to higher frequencies was observed even at Γ and Y points. Since our nanowires are relatively large, they present densely packed modes. Here, we sufficed to the frequencies below 2 THz for illustration purposes and a figure up to 10 THz is placed in the supplementary material (Fig. S1). It indicates that a change in D_{core} between 0 and 4 nm shifts the upper boundary from 7.7 to 9.25 THz. For pure InAs, there is also a gap at 5.27–5.53 THz that immediately vanishes upon introducing the GaAs core.

C. Phonon density of states

Figure 4 shows the longitudinal and transverse PDOS for nanowires with hexagonal and triangular shells and various D_{core}. The similarity between longitudinal and transverse PDOS increases the probability of coupling between these modes reported by others.[21,22] A systematic transition can be seen upon the change in D_{core} for all geometries. In particular, the InAs major peak at 6.5 THz gradually decays and gives rise to the GaAs major peak at 8.8 THz. Note that the blue and brown solid curves in (a) indicate pure InAs and pure GaAs, respectively. Starting with the difference between longitudinal and transverse modes, the overlapping peaks around 8 THz that intensified InAs major peaks [(a) and (c)] unmerged and shifted toward GaAs major peaks in (b) and (d). This is more evident for D_{core} = 3 nm indicated by red but to some extent present in all curves. With regard to the shell geometry, one can see more separation between InAs and GaAs peaks for both longitudinal and transverse cases. For instance, consider D_{core} = 3 nm (red solid curves) where the GaAs peak appears as a small step in (a), but it is more clear in (c). Similarly, the separation between red peaks in (b) becomes wide and clear in (d).

Finally, for D_{core} = 1 and 2 nm, the importance of matching, indicated by solid and dashed lines, is negligible, while for larger core diameters, it is more pronounced. The effect of corner-matching can be summarized as a slight increase in the intensity of InAs major peaks and a simultaneous reduction in the intensity of GaAs major peaks. The result for different parameters such as nanowire length, diameters, and sampling is presented in Sec. S3 of the supplementary material. Considering the integral of PDOS as the available phonon subbands,[55] one can expect the lowest κ for the 4 nm GaAs@5 nm InAs nanowire in all cases.

D. Thermal conductivity

Figure 5 shows the change in κ with D_{core} determined by EMD, NEMD, and rNEMD methods at 300 K. It can be seen that all methods predict a minimum in κ with the change in D_{core}. Similar minima upon variation of the shell thickness for Ge@Si and GaAs@AlAs nanowires[22,56] and the shell composition in $Si@Ge_xSi_{1-x}$ nanowires[23] have earlier been reported, which were attributed to localization of low-frequency modes at the interface. Within the harmonic approximation, replacing heavy In with Ga,

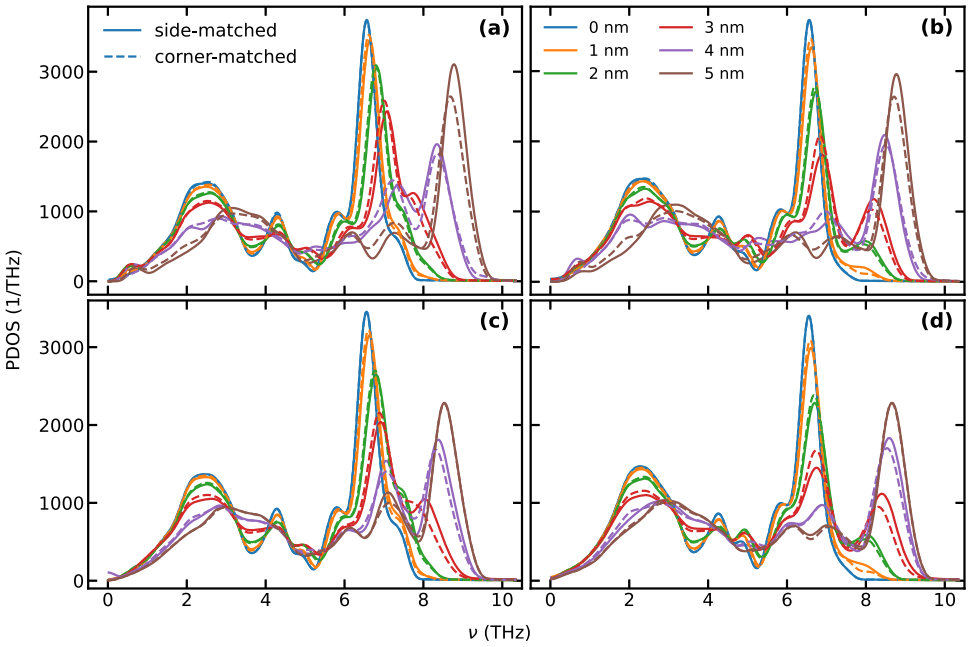

FIG. 4. The result of PDOS in the [(a) and (c)] longitudinal and [(b) and (d)] transverse direction for nanowires with the [(a) and (b)] 5 nm hexagonal shell and [(c) and (d)] 7 nm triangular shell at 300 K. The solid and dashed lines denote the matching, while the colors indicate hexagonal core diameters for all subplot.

which has a closer mass to that of As, might improve κ. This means one can expect a monotonic increase in κ with the increase in D_{core}. However, the minimum in our results is an indication of an anharmonic behavior namely due to the presence of interfacial strain. It has been shown that strain can lead to changes in group velocity and increased scattering in GaAs.[57] However, this effect is localized and vanishes away from the interface.[17]

It is also worth mentioning that although side- and corner-matched geometry attracted the attention of the experimental community, we cannot see any systematic difference in terms of their κ. For NEMD and rNEMD, even the shell geometry is unimportant. However, EMD predicts lower κ for the triangle shell although we maintained the cross-sectional area when changing the shell geometry. This is quite opposite to what has been observed in Si–Ge core–shell nanowires.[15] As mentioned in the introduction, the lattice mismatch is larger for GaAs/InAs and their bulk κ is less than half Si/Ge. For these reasons, we did not expect GaAs/InAs to behave same as Si/Ge.

In the case of EMD, Fig. 5(a), the minima for hexagonal and triangular geometries coincide with the maximum interface area. A further increase in D_{core} causes the interface to become discontinuous and increases κ accordingly. The point with the largest κ in Fig. 5(a) represents the pure GaAs nanowire without interface. It is worth noting that pure GaAs is also the most relaxed case in Fig. 2.

The minima occur at 2–3 nm for the NEMD and 1–3 nm for the rNEMD method, Figs. 5(b) and 5(c), respectively. Thus, the minima are slightly shifted to lower D_{core} using NEMD, but they are more clearly shifted using rNEMD. In addition, κ of NEMD is almost twice rNEMD and four times higher than that of the EMD approach. One might blame the EMD method for yielding such low κ values. In fact, an incorrect definition of the heat current when employing a three-body potential can lead to an underestimation of κ in EMD.[40,58] Note that the textbook expression of heat current remains valid for pair potentials, such as Lennard–Jones. Using the Tersoff potential, Khadem and Wemhoff[58] demonstrated that the EMD results are dependent on the specific heat current formula, with some showing agreement with the NEMD ones. Later, Fan *et al.*[40] corrected the heat current expression for many-body potentials. Here, we used their definition in our EMD calculations as implemented in `GPUMD`.

Further validation of the EMD results can be achieved by comparison with experimental data. Persson *et al.*[59] applied effective medium theory to the measurement of a vertical array and estimated κ of 5.3 ± 1.7 W/mK for the 52 nm InAs nanowire. Zhou *et al.*[4] reported 7.3 W/mK for an individual hexagonal InAs nanowire of 63 nm in diameter. Swinkels *et al.*[60] measured κ of individual nanowires laid on SiN and reported 4.5 W/mK for 40 nm InAs after removing substrate effect. Fust *et al.*[11] obtained ~3 W/mK for the 15–40 nm GaAs core in the GaAlAs shell. At first glance, one may consider κ of NEMD and rNEMD as a better estimation. However, experimentally measured diameters are much larger than the nanowires studied here. Furthermore, both theoretical and experimental evidence suggest a reduction in κ with the decrease in the diameter of nanowires .[61] For this reason, we consider EMD results to be more accurate and the NEMD and rNEMD results seem to be very high for the nanowires studied here. Thus, in the following, we discuss parameters proposed in the literature that may affect κ determined by the NEMD approach.

The dependence of κ on the nanowire L has been validated by both experimental studies and NEMD simulations, cf. Ref. 62, which indicate that κ increases with L before reaching a saturation point. In this study, we used the same L for the method comparison. For completeness, results for different L values are provided in Fig. S8 of the supplementary material. Within the studied range

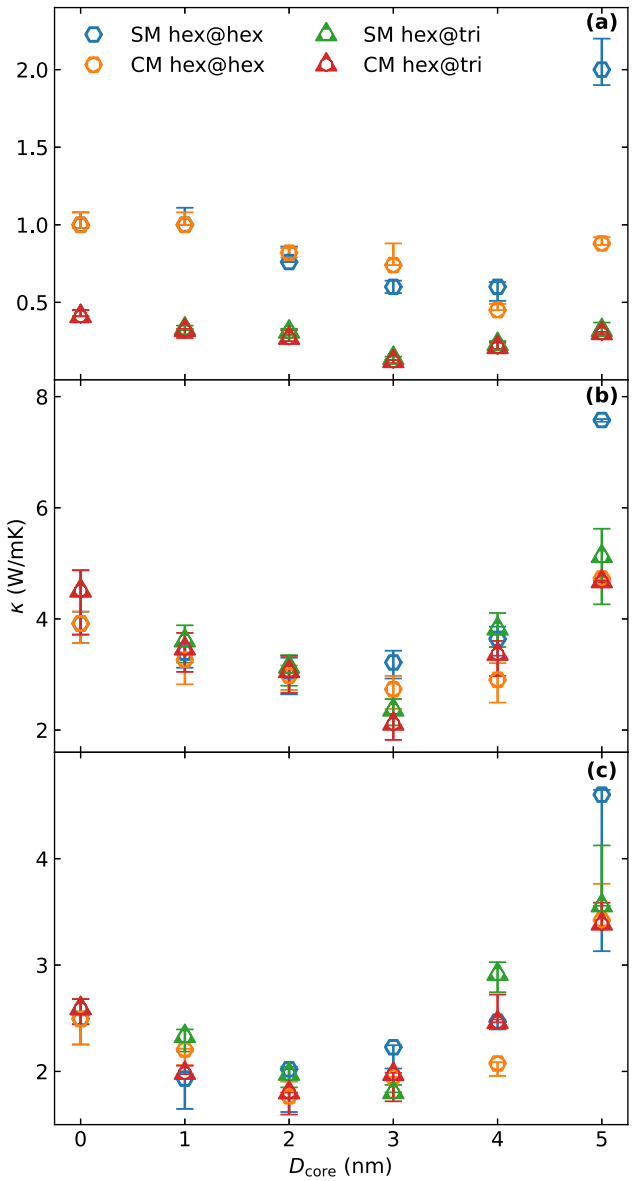

FIG. 5. Variation of κ with the core diameter at 300 K determined by (a) EMD, (b) NEMD, and (c) rNEMD. The legend in (a) indicates the nanowire's geometry where SM/CM denotes side-matched/corner-matched and hex/tri stands for hexagon/triangle.

(up to 1 μm), the NEMD κ continues to increase. The increase implies that long-wavelength phonon modes have a significant contribution to thermal conductivity. Matching the NEMD κ to that of EMD would require nanowire lengths of only a few nanometers, which is not realistic.

Another point of debate in the literature is the choice of force field. Carrete *et al.*[17] calculated κ of InAs, GaAs, and InP nanowires, comparing the Tersoff and Vashishta potentials with the Harrison potential, which includes only harmonic bonds and angles. They found that using the NEMD approach, the Tersoff and Vashishta potentials predict κ values an order of magnitude higher than the Harrison potential. However, Tersoff and Vashishta were deemed more reliable for small nanowires, as in the present study, primarily due to their non-symmetric potential wells. In contrast, simpler potentials such as Harrison are more suitable for larger nanowires on the order of tens of nanometers in diameter, where computational efficiency or the harmonic approximation is of concern.

A typical NEMD temperature profile might be non-linear near the thermostated regions, and thus, it is a common practice to exclude those regions from ΔT and L when κ is calculated (see Fig. S11 of the supplementary material). Li *et al.*[49] compared Nosé–Hoover and Langevin thermostats and suggested that when Langevin is used, the imposed ΔT and whole system length predict a correct κ. However, even when considering the error bars, the NEMD and rNEMD results remain significantly higher than the EMD results. We would like to highlight that the length dependence of the NEMD and rNEMD methods for the hexagonal core, and the side-matched case is shown in Figs. S8 and S12 of the supplementary material. Although κ is higher, both methods show that agreement with the EMD minima at D_{core} = 4 nm can be achieved with an increase in length.

Regardless of the method proposed for unifying EMD, NEMD, and rNEMD results, there is agreement on the non-equilibrium contribution to κ, e.g., heat bath contribution in the NEMD as a source of difference.[49] We try to elucidate and discuss these effects using the temperature-dependent study. Briefly, κ behavior for the bulk can be divided into two portions below Debay temperature (Θ_D) where the scattering rate is low and $\kappa \propto T^3$ and above that dominated by *Umklapp* scattering with $\kappa \propto T^{-1}$. In between, κ reaches a peak, e.g., 10–20 K for the bulk InAs[32] and 15–40 K in the case of bulk GaAs.[30] For nanowires, *boundary* scattering is also present at the surface that affects long-wavelength modes at low temperatures. In addition, saturation of Umklapp scattering is expected at high temperatures ($>T_{sat}$) due to strong phonon–phonon interaction mediated by confinement. It has been predicted by BTE modeling that Umklapp scattering becomes dominant over boundary scattering at 270 K for large (125 nm) defect-free InAs nanowires.[9] This temperature is expected to increase with a decrease in nanowire diameter. Nonetheless, Umklapp scattering and boundary scattering cause a peak 80–90 K for 125 nm InAs. Although their BTE model has been verified by fitting experimental data, it may still fail at a smaller scale.[16,55] For instance, the shift of peak to higher temperature upon a decrease in nanowire diameter has been experimentally observed for Si nanowires of 22–115 nm.[63] To fit the latter result by BTE, Mingo *et al.*[55] showed that only phonon dispersion obtained by MD simulation presents a reasonable agreement. However, they could not fit the smallest Si nanowire (22 nm), which suggests that measurement and analysis of ultra-thin nanowires are challenging.

Figure 6 shows the temperature-dependent behavior of κ obtained by EMD, NEMD, and rNEMD, respectively. The EMD results in Figs. 6(a) and 6(b) show the T^{-1} decay, which is characteristic of Umklapp scattering being dominant. Additionally, as temperature increases, the distribution of results narrows. A similar trend, with results converging at higher temperatures and approaching a lower limit, has been observed in Si–Ge nanowires using

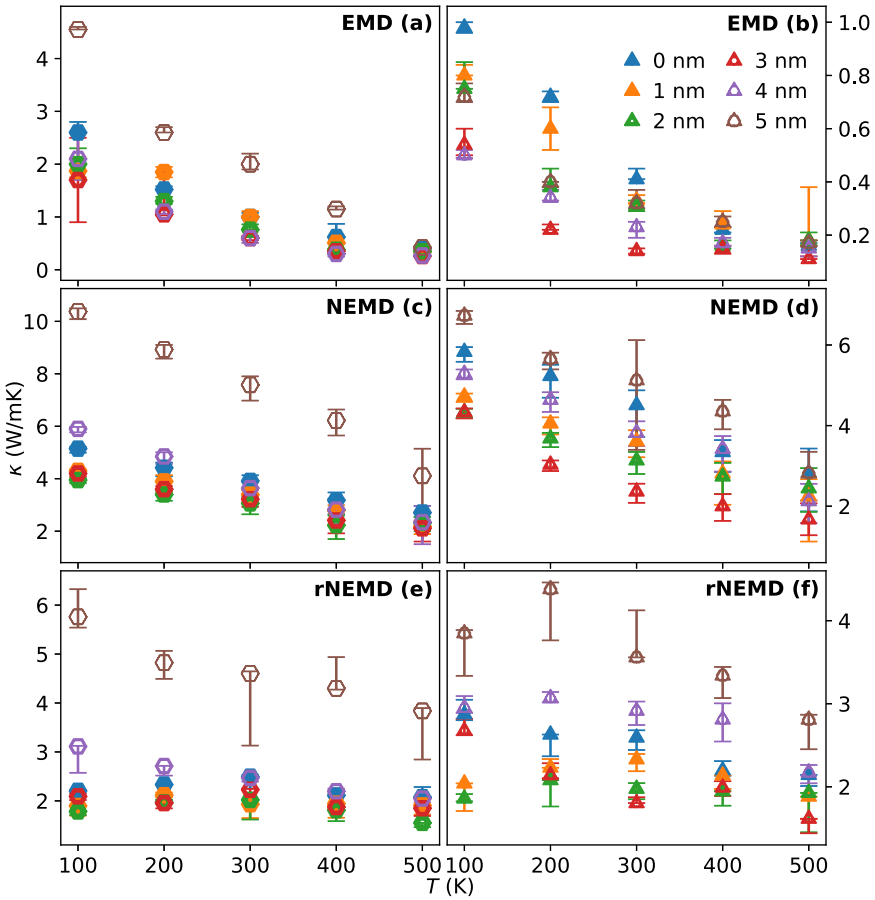

FIG. 6. Variation of κ obtained by [(a) and (b)] EMD, [(c) and (d)] NEMD, and [(e) and (f)] rNEMD with temperature and D_{core} for [(a), (c), and (e)] hexagonal and [(b), (d), and (f)] triangular shells with side-matched geometry. The legend in (b) is valid for all subplots.

EMD.[24] Overall, nanowires with D_{core} = 4 nm among the hexagonal shells, Fig. 6(a), and nanowires with the 3 nm core for the triangular ones, Fig. 6(b), present the least κ and lower T_{sat}. These nanowires also present maximum interface areas, suggesting that interface scattering is present alongside the boundary scattering from low temperatures. For the rest of the nanowires, reaching the lower limit is postponed to higher temperatures due to weaker interface scattering. Note that the lower limit itself indicates the saturation of Umklapp scattering because it occurs for pure InAs and GaAs without the interface. However, since stronger interface scattering reduces T_{sat}, it suggests that interface scattering behaves as phonon–phonon scattering rather than typical boundary scattering. This is in agreement with modal analysis where localization of the low-frequency mode at the interface has been demonstrated.[22,23] This is very interesting because earlier it has been widely accepted that phonon–phonon scattering can be neglected at low temperatures. Here, we show that interface scattering is present, even at low temperatures, and can interact with low energy modes.

Using the NEMD method, we observe a linear behavior rather than T^{-1} decay for all datasets shown in Figs. 6(c) and 6(d). Note that the noise from the heat bath[54] is larger at higher temperatures. However, even at 100 K, the NEMD result does not agree with that of EMD, which implies that baths are pumping either low- or high-energy modes, leading to an overestimation of κ. However, unlike EMD, the results here do not converge at high temperatures, meaning that the saturation of Umklapp scattering does not occur within 100–500 K. Thus, the heat flux primarily consists of low-energy modes, which are less susceptible to Umklapp scattering, and the thermostats predominantly pump these low-energy modes. Since interface scattering primarily affects low-energy phonons, provided by thermostats, the distribution of results remains consistent across the range of studied temperatures. To verify our hypothesis, we determined the spectral thermal conductance, a beneficial method for further analysis of the NEMD results.[49] The methodology for calculating the spectrally decomposed conductance is detailed in Sec. S5 of the supplementary material. As shown in Fig. S9 of the supplementary material, the results exhibit a peak at $\frac{\omega}{2\pi}$ = 2.5–4.5 THz, indicating that low-energy modes are being dominant in the 100–500 K range. This is a clear proof of our theorem on the contribution of thermostats through low-energy modes. To mitigate this artifact, we compared the spectral thermal conductance for different L while maintaining a consistent temperature gradient (20 K/100 nm). As illustrated in Fig. S10 of the supplementary material, this artifact can be effectively reduced by increasing the system length. The Langevin thermostat's tendency to pump low-frequency modes has also been observed in asymmetric carbon

nanotubes.[64] Previously, it has been criticized for broadening PDOS peaks and smoothing out the phonon distribution.[65]

In rNEMD results shown in Figs. 6(e) and 6(f), one can observe the κ decay and, for some nanowires, the peak before decay, which were missing in the EMD and NEMD results. Vuttivorakulchai *et al.*[9] predicted a peak in κ at 200–300 K using BTE for large-diameter InAs nanowires, considering the boundary and Umklapp scattering. However, as previously noted, BTE predictions may not accurately capture the behavior of ultrathin nanowires.[16,55] Furthermore, in addition to the boundary and Umklapp scattering, interface scattering must be considered in the BTE model.[16] Thus, the peak observed in the rNEMD results is likely an artifact. It has been widely accepted that the swapping of energy between cold and hot regions can disproportionately affect phonon modes. The bias of rNEMD toward low-frequency phonon modes has been shown to result in κ values up to 1000 W/mK higher than those obtained using the EMD approach for single-walled carbon nanotubes.[66] However, the observed peak here is most likely attributed to energy exchanges that excite high-frequency phonon modes. As mentioned earlier, high-frequency phonon modes are primarily responsible for the increase in κ, reaching a peak and decay within the bulk state. We believe a similar phenomenon occurs here, with high-energy modes being artificially introduced through energy swaps.

Unfortunately, spectral analysis cannot be applied to the rNEMD method, and thus, we are unable to quantitatively demonstrate the artifact. Instead, we repeated rNMED calculation for longer nanowires, which shows saturation of κ around L = 100 nm (see Fig. S12 of the supplementary material) in agreement with an earlier study.[17] Since κ obtained by the rNEMD method saturates at a much smaller length compared to NEMD, this indicates that low-frequency phonon modes are not dominating the heat transport in the rNEMD approach.

IV. SUMMARY

To summarize, we showed that within the GaAs@InAs core–shell nanowires, κ is strongly affected by the interface regardless of the nanowire cross-sectional geometry, suggesting the importance of interface scattering. Using the existing methods for the calculation of κ in the MD framework, we have shown that κ presents a minimum with respect to D_{core}. The minimum is of particular importance for increasing the thermoelectric figure of merit. However, the minima occur at larger D_{core} for the EMD approach and shift to smaller D_{core} using NEMD and rNEMD. In addition, both NEMD and rNEMD approaches predict significantly higher κ values than EMD, a discrepancy that cannot be resolved using existing corrections in the literature. The EMD temperature-dependent analysis indicates that interface scattering presents phonon–phonon interaction characteristics, resembling Umklapp scattering rather than boundary scattering, likely due to the localization of low-frequency modes at the interface. The latter finding is confirmed by NEMD results, although the Langevin thermostat exhibits a bias toward low-frequency modes, leading to higher κ values, as demonstrated by spectral heat conductance analysis. This artifact diminishes with the increasing nanowire length, although longer nanowires also elevate κ values. Unlike EMD and NEMD, rNEMD may predict a κ peak with temperature, akin to high-frequency phonon effects observed in bulk materials. In addition, saturation of κ at shorter lengths implies lesser influence from low-energy modes.

Overall, modeling κ in core–shell nanowires presents challenges due to their sensitivity to both low- and high-frequency phonon modes. Our findings suggest that EMD yields more reliable κ values, albeit requiring extensive simulation iterations to converge. Nevertheless, a combination of methods is recommended to develop a more comprehensive understanding of thermal transport mechanisms in such systems.

SUPPLEMENTARY MATERIAL

Extra details on the calculation of atomistic stress phonon dispersion and spectral heat conductance as well as supporting figures are presented in the supplementary material.

ACKNOWLEDGMENTS

This work was supported by the Icelandic Research Fund, Grant No. 195943-051. Computations were performed at C3SE Vera provided by Chalmers e-Commons.

AUTHOR DECLARATIONS

Conflict of Interest

The authors have no conflicts to disclose.

Author Contributions

Alireza Seifi: Conceptualization (equal); Data curation (equal); Formal analysis (equal); Funding acquisition (equal); Investigation (equal); Methodology (equal); Project administration (equal); Resources (equal); Software (equal); Supervision (equal); Validation (equal); Visualization (equal); Writing – original draft (equal); Writing – review & editing (equal). **Mahyar Ghasemi**: Data curation (equal); Formal analysis (equal); Methodology (equal); Project administration (equal); Software (equal); Visualization (equal); Writing – original draft (equal). **Movaffaq Kateb**: Conceptualization (equal); Funding acquisition (equal); Investigation (equal); Methodology (equal); Resources (equal); Supervision (equal); Validation (equal); Writing – original draft (equal); Writing – review & editing (equal). **Pirooz Marashi**: Conceptualization (equal); Data curation (equal); Formal analysis (equal); Investigation (equal); Methodology (equal); Project administration (equal); Resources (equal); Software (equal); Supervision (equal); Visualization (equal); Writing – original draft (equal); Writing – review & editing (equal).

DATA AVAILABILITY

The data that support the findings of this study are available from the corresponding author upon reasonable request.

REFERENCES

[1] G. J. Snyder and E. S. Toberer, "Complex thermoelectric materials," in *Materials for Sustainable Energy* (World Scientific & Nature Publishing Group, 2011), pp. 101–110.
[2] R. Kim, S. Datta, and M. S. Lundstrom, J. Appl. Phys. **105**, 034506 (2009).
[3] S. A. Dayeh, D. P. R. Aplin, X. Zhou, P. K. L. Yu, E. T. Yu, and D. Wang, Small **3**, 326 (2007).
[4] F. Zhou, A. L. Moore, J. Bolinsson, A. Persson, L. Fröberg, M. T. Pettes, H. Kong, L. Rabenberg, P. Caroff, D. A. Stewart *et al.*, Phys. Rev. B **83**, 205416 (2011).
[5] Y. Tian, M. R. Sakr, J. M. Kinder, D. Liang, M. J. MacDonald, R. L. J. Qiu, H.-J. Gao, and X. P. A. Gao, Nano Lett. **12**, 6492 (2012).
[6] P. M. Wu, J. Gooth, X. Zianni, S. F. Svensson, J. G. Gluschke, K. A. Dick, C. Thelander, K. Nielsch, and H. Linke, Nano Lett. **13**, 4080 (2013).
[7] P. Mensch, S. Karg, V. Schmidt, B. Gotsmann, H. Schmid, and H. Riel, Appl. Phys. Lett. **106**, 093101 (2015).
[8] S. G. Jeon, D. W. Park, H. S. Shin, H. M. Park, S. Y. Choi, S. J. Lee, J. Yu, and J. Y. Song, RSC Adv. **6**, 7791 (2016).
[9] K. Vuttivorakulchai, M. Luisier, and A. Schenk, J. Appl. Phys. **124**, 205101 (2018).
[10] J. W. W. van Tilburg, R. E. Algra, W. G. G. Immink, M. Verheijen, E. P. A. M. Bakkers, and L. P. Kouwenhoven, Semicond. Sci. Technol. **25**, 024011 (2010).
[11] S. Fust, A. Faustmann, D. J. Carrad, J. Bissinger, B. Loitsch, M. Döblinger, J. Becker, G. Abstreiter, J. J. Finley, and G. Koblmüller, Adv. Mater. **32**, 1905458 (2020).
[12] S. I. Erlingsson, A. Manolescu, G. A. Nemnes, J. H. Bardarson, and D. Sanchez, Phys. Rev. Lett. **119**, 036804 (2017).
[13] H. Rezaie Heris, M. Kateb, S. I. Erlingsson, and A. Manolescu, Nanotechnology **31**, 424006 (2020).
[14] H. Rezaie Heris, M. Kateb, S. I. Erlingsson, and A. Manolescu, in *CMD2020GEFES* (European Physical Society, Madrid, 2020), p. 49081, https://eventos.uam.es/_files/_event/_28512/papers/49081/Heat_transport_by_electrons_and_phonons_in_tubular_nanowires_1.docx.
[15] H. R. Heris, M. Kateb, S. I. Erlingsson, and A. Manolescu, Surf. Interfaces **30**, 101834 (2022).
[16] M. C. Wingert, Z. C. Y. Chen, E. Dechaumphai, J. Moon, J.-H. Kim, J. Xiang, and R. Chen, Nano Lett. **11**, 5507 (2011).
[17] J. Carrete, R. C. Longo, and L. J. Gallego, Nanotechnology **22**, 185704 (2011).
[18] W.-X. Zhou, K.-Q. Chen, L.-M. Tang, and L.-J. Yao, Phys. Lett. A **377**, 3144 (2013).
[19] Y.-Y. Liu, W.-X. Zhou, L.-M. Tang, and K.-Q. Chen, Appl. Phys. Lett. **103**, 263118 (2013).
[20] M. Hu, K. P. Giapis, J. V. Goicochea, X. Zhang, and D. Poulikakos, Nano Lett. **11**, 618 (2011).
[21] J. Chen, G. Zhang, and B. Li, J. Chem. Phys. **135**, 104508 (2011).
[22] J. Chen, G. Zhang, and B. Li, Nano Lett. **12**, 2826 (2012).
[23] G. Xie, B. Li, L. Yang, J. Cao, Z. Guo, M. Tang, and J. Zhong, J. Appl. Phys. **113**, 083501 (2013).
[24] S. Sarikurt, A. Ozden, A. Kandemir, C. Sevik, A. Kinaci, J. B. Haskins, and T. Cagin, J. Appl. Phys. **119**, 155101 (2016).
[25] J. C. Thompson and B. A. Younglove, J. Phys. Chem. Solids **20**, 146 (1961).
[26] C. J. Glassbrenner and G. A. Slack, Phys. Rev. **134**, A1058 (1964).
[27] J. A. Carruthers, T. H. Geballe, H. M. Rosenberg, and J. M. Ziman, Proc. R. Soc. A **238**, 502 (1957).
[28] G. A. Slack and C. Glassbrenner, Phys. Rev. **120**, 782 (1960).
[29] A. S. Okhotin, A. S. Pushkarskii, and V. V. Gorbachev, *Thermophysical Properties of Semiconductors* (Atomizdat, Moscow, 1972).
[30] R. O. Carlson, G. A. Slack, and S. J. Silverman, J. Appl. Phys. **36**, 505 (1965).
[31] J. S. Blakemore, J. Appl. Phys. **53**, R123 (1982).
[32] P. Tamarin and S. Shalyt, Sov. Phys. Semicond. **5**, 1097 (1971).
[33] M. Hu, X. Zhang, K. P. Giapis, J. V. Goicochea, and D. Poulikakos, "Thermal conductivity reduction in core-shell nanowires," Phys. Rev. B **84**(8), 085442 (2011).
[34] D. J. O. Göransson, M. Heurlin, B. Dalelkhan, S. Abay, M. E. Messing, V. F. Maisi, M. T. Borgström, and H. Q. Xu, Appl. Phys. Lett. **114**, 053108 (2019).
[35] Ö. Gül, H. Y. Günel, H. Lüth, T. Rieger, T. Wenz, F. Haas, M. Lepsa, G. Panaitov, D. Grützmacher, and Th. Schäpers, Nano Lett. **14**, 6269 (2014).
[36] S. Plimpton, J. Comput. Phys. **117**, 1 (1995).
[37] Z. Fan, W. Chen, V. Vierimaa, and A. Harju, Comput. Phys. Commun. **218**, 10 (2017).
[38] J. Tersoff, Phys. Rev. B **37**, 6991 (1988).
[39] Z. Fan, H. Dong, A. Harju, and T. Ala-Nissila, Phys. Rev. B **99**, 064308 (2019).
[40] Z. Fan, L. F. C. Pereira, H.-Q. Wang, J.-C. Zheng, D. Donadio, and A. Harju, Phys. Rev. B **92**, 094301 (2015).
[41] T. Hammerschmidt, P. Kratzer, and M. Scheffler, Phys. Rev. B **77**, 235303 (2008).
[42] L. Verlet, Phys. Rev. **159**, 98 (1967).
[43] J. M. Dickey and A. Paskin, Phys. Rev. **188**, 1407 (1969).
[44] M. S. Green, J. Chem. Phys. **22**, 398 (1954).
[45] R. Kubo, J. Phys. Soc. Jpn. **12**, 570 (1957).
[46] F. Müller-Plathe, J. Chem. Phys. **106**, 6082 (1997).
[47] S.-c. Wang, X.-g. Liang, X.-h. Xu, and T. Ohara, J. Appl. Phys. **105**, 014316 (2009).
[48] R. E. Brophy, M. Kateb, K. Torfason, G. A. Nemnes, H. G. Svavarsson, I. Pintilie, and A. Manolescu, J. Phys. Chem. C **127**, 7938 (2023).
[49] Z. Li, S. Xiong, C. Sievers, Y. Hu, Z. Fan, N. Wei, H. Bao, S. Chen, D. Donadio, and T. Ala-Nissila, J. Chem. Phys. **151**, 234105 (2019).
[50] A. Stukowski, Modell. Simul. Mater. Sci. Eng. **18**, 015012 (2009).
[51] W.-X. Zhou, S. Tan, K.-Q. Chen, and W. Hu, J. Appl. Phys. **115**, 124308 (2014).
[52] J. Chen, Z. Hou, H. Chen, and Z. Wang, J. Phys.: Condens. Matter **34**, 445301 (2022).
[53] Z. Fan, L. F. C. Pereira, P. Hirvonen, M. M. Ervasti, K. R. Elder, D. Donadio, T. Ala-Nissila, and A. Harju, Phys. Rev. B **95**, 144309 (2017).
[54] M. Salmani-Jelodar, A. Paul, T. Boykin, and G. Klimeck, J. Comput. Electron. **11**, 22 (2012).
[55] N. Mingo, L. Yang, D. Li, and A. Majumdar, Nano Lett. **3**, 1713 (2003).
[56] T. Juntunen, T. Koskinen, V. Khayrudinov, T. Haggren, H. Jiang, H. Lipsanen, and I. Tittonen, Nanoscale **11**, 20507 (2019).
[57] A. Vega-Flick, D. Jung, S. Yue, J. E. Bowers, and B. Liao, Phys. Rev. Mater. **3**, 034603 (2019).
[58] M. H. Khadem and A. P. Wemhoff, Comput. Mater. Sci. **69**, 428 (2013).
[59] A. I. Persson, Y. K. Koh, D. G. Cahill, L. Samuelson, and H. Linke, Nano Lett. **9**, 4484 (2009).
[60] M. Y. Swinkels, M. R. van Delft, D. S. Oliveira, A. Cavalli, I. Zardo, R. W. van der Heijden, and E. P. A. M. Bakkers, Nanotechnology **26**, 385401 (2015).
[61] N. Mingo and D. A. Broido, Phys. Rev. Lett. **93**, 246106 (2004).
[62] X. Xu, L. F. C. Pereira, Y. Wang, J. Wu, K. Zhang, X. Zhao, S. Bae, C. Tinh Bui, R. Xie, J. T. L. Thong *et al.*, Nat. Commun. **5**, 3689 (2014).
[63] D. Li, Y. Wu, P. Kim, L. Shi, P. Yang, and A. Majumdar, Appl. Phys. Lett. **83**, 2934 (2003).
[64] W.-J. Chen, B. Feng, C. Shao, J. Yang, L. Fan, W.-L. Ong, and I.-L. Chang, Int. J. Heat Mass Transfer **184**, 122341 (2022).
[65] J. Dunn, E. Antillon, J. Maassen, M. Lundstrom, and A. Strachan, J. Appl. Phys. **120**, 225112 (2016).
[66] E. A. Walker, "Influence of phonon modes on the thermal conductivity of single-wall, double-wall, and functionalized carbon nanotubes," Ph.D. thesis, Vanderbilt University, 2012, University of Example.